ACS APPLIED MATERIALS & INTERFACES

www.acsami.org Research Article

Determination of Hafnium Zirconium Oxide Interfacial Band Alignments Using Internal Photoemission Spectroscopy and X-ray Photoelectron Spectroscopy

Melanie A. Jenkins, Konner E. K. Holden, Sean W. Smith, Michael T. Brumbach, M. David Henry, Conan Weiland, Joseph C. Woicik, Samantha T. Jaszewski, Jon F. Ihlefeld, and John F. Conley, Jr.*

Cite This: *ACS Appl. Mater. Interfaces* 2021, 13, 14634−14643 Read Online

ACCESS | Metrics & More | Article Recommendations | Supporting Information

ABSTRACT: Doped ferroelectric HfO_2 is highly promising for integration into complementary metal-oxide semiconductor (CMOS) technology for devices such as ferroelectric nonvolatile memory and low-power field-effect transistors (FETs). We report the direct measurement of the energy barriers between various metal electrodes (Pt, Au, Ta, TaN, Ti/Pt, Ni, Al) and hafnium zirconium oxide ($Hf_{0.58}Zr_{0.42}O_2$, HZO) using internal photoemission (IPE) spectroscopy. Results are compared with valence band offsets determined using the three-sample X-ray photoelectron spectroscopy (XPS) as well as the two-sample hard X-ray photoelectron spectroscopy (HAXPES) techniques. Both XPS and IPE indicate roughly the same dependence of the HZO barrier on metal work function with a slope of 0.8 ± 0.5. XPS and HAXPES-derived barrier heights are on average about 1.1 eV smaller than barrier heights determined by IPE, suggesting the presence of negative charge in the HZO.

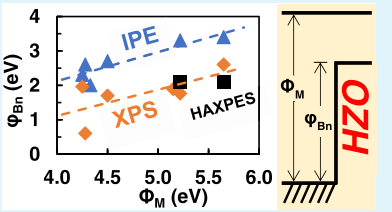

KEYWORDS: *internal photoemission spectroscopy, X-ray photoelectron spectroscopy, hafnium zirconium oxide, ferroelectric, energy barriers*

INTRODUCTION

Ferroelectric materials based on HfO_2 have been highly researched in recent years for multiple microelectronic applications. One application with a large degree of recent interest is the use of ferroelectric materials in negative capacitance field-effect transistors (FETs) to achieve subthreshold swings steeper than the thermionic limit of 60 mV/decade for conventional FETs.[1] Ferroelectric materials, including HfO_2, have demonstrated negative differential capacitance[2,3] and FinFET structures utilizing these materials have exhibited subthreshold slopes less than 60 mV/decade.[4] Other potential applications are for nonvolatile memory, such as ferroelectric random access memory (FRAM)[5] and ferroelectric tunnel junctions (FTJs).[6] Compared to traditional ferroelectrics, such as lead zirconate titanate, HfO_2-based ferroelectric materials are of particular interest due to the ease of integration with existing silicon CMOS processing, where HfO_2-based materials are already used for the gate dielectric. Ferroelectricity in HfO_2 has been attributed to a metastable noncentrosymmetric orthorhombic phase.[7] The stability of this phase can be improved with a number of dopants, one of which is zirconium,[8−10] where the relative ratio of Zr to Hf may be used to control the ratio of phases present and thus the dielectric response.[11] The lower annealing requirements, strong polarization response, and broad orthorhombic phase composition range of zirconium doping of HfO_2 ($Hf_{1-x}Zr_xO_2$ or HZO) make it an attractive choice for device applications.[12]

Successful integration of HZO materials into memories or FETs necessitates an understanding of the band offsets of these materials with various electrodes. According to the zero-order Schottky−Mott rule, the band offset or barrier, φ_{Bn}, between the Fermi level of the metal, E_{FM}, and the conduction band of an insulator should vary as $\varphi_{Bn} = \Phi_{M,vac} - \chi_i$, where $\Phi_{M,vac}$ is the vacuum work function of the metal and χ_i is the electron affinity of the insulator. In practice, however, this is typically not the case.[13,14] Metal-induced gap state (MIGS) theory, a more advanced theory that considers charge transfer into intrinsic (metal induced) interface traps (the gap states), predicts the formation of an interfacial dipole that drives E_{FM} toward the charge-neutral level of the insulator, $E_{CNL,i}$. $E_{CNL,i}$ is the energy at which the dominant character of the interface traps states switches from donor-like in the lower part of the gap to acceptor-like in the upper. This can result in Fermi level "pinning" or insensitivity of φ_{Bn} to $\Phi_{M,vac}$. Pinning is, in general, enhanced for high dielectric constant (κ) materials,[15−17] of which $Hf_{1-x}Zr_xO_2$ could be categorized, and would result in less control over threshold voltage of ferroelectric-

Received: October 2, 2020
Accepted: March 10, 2021
Published: March 22, 2021

https://doi.org/10.1021/acsami.0c17729
ACS Appl. Mater. Interfaces 2021, 13, 14634−14643

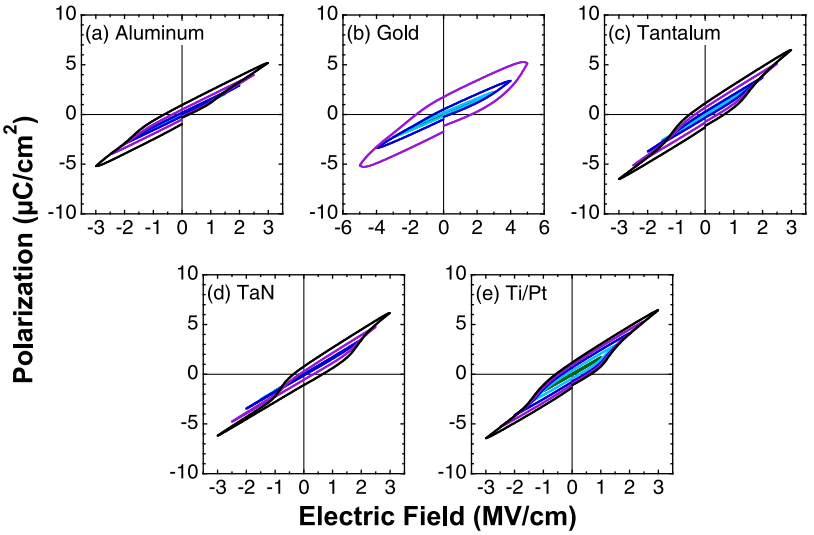

Figure 1. Polarization-field response for metal/HZO/TaN capacitors with (a) aluminum, (b) gold, (c) tantalum, (d) TaN, and (e) Ti/Pt top metal contacts.

based transistors. In addition to dipoles due to induced interface traps, other nonidealities such as dipoles due to interfacial chemical reactions and scavenging of oxygen, interface and oxide trapped charge due to point defects,[18] and interfacial layers due to reactive electrodes can also cause observed band offsets to deviate substantially from ideal calculated values. All of these nonidealities are affected by process details such as the deposition method, subsequent anneals, and specific material interfaces. Thus, it is beneficial for integration efforts to characterize the barrier height between various metals and the HZO material. Techniques to measure barrier heights include X-ray photoelectron spectroscopy (XPS), hard X-ray photoelectron spectroscopy (HAXPES), and internal photoemission (IPE) spectroscopy. Although XPS is widely used and can assess valance band offsets between adjacent materials, IPE is the only technique capable of direct measurement of the barrier heights inside an actual working device structure.[14,19,20] HfO_2 and ZrO_2 in metal/oxide/semiconductor (MOS) devices have been extensively characterized with IPE. To date, however, there are few previous reports of IPE of metal/insulator/metal (MIM) devices,[13,21−24] and no previous IPE reports measuring the energy barriers between $Hf_{1-x}Zr_xO_2$ materials with compositions and processing conditions that may stabilize the ferroelectric phase and various metals.

In this work, we use IPE to directly measure the metal Fermi level to conduction band barrier heights of six commonly used metals (Pt, Au, Ta, TaN, Ti/Pt, and Al) in direct contact with $Hf_{1-x}Zr_xO_2$ in functioning MIM capacitors. We compare the IPE results with XPS and HAXPES measurements of valence band offsets in several of these systems. Although polarization magnitudes measured in these samples are less than expected (due to the processing limitations imposed by the IPE sample requirements), the barrier differences observed here may be clearly attributed to the electrode/HZO electronic structure and should prove valuable for HZO device design.

EXPERIMENTAL SECTION

Metal/insulator/metal capacitor structures were fabricated for IPE measurements of barrier heights. First, a 100 nm thick TaN blanket bottom electrode was deposited via pulsed DC sputtering from a TaN target on lightly doped Si substrates with a native oxide. Then, HZO was deposited in an Ultratech Savannah S100 flow-through style atomic layer deposition (ALD) system at 150 °C using tetrakis-(dimethylamino)hafnium (TDMA-Hf, held at 75 °C) and tetrakis-(dimethylamino)zirconium (TDMA-Zr, held at 75 °C), with H_2O (held at ∼40 °C) as the oxidizing agent for both. A 20 nm thick HZO film was deposited using 102 ALD supercycles, each comprising 1 ZrO_2 cycle (0.25 s TDMA-Z/30 s N_2/0.015 s H_2O/30 s N_2) and 1 HfO_2 cycle (0.15 s TDMA-H/30 s N_2/0.015 s H_2O/30 s N_2).[11] The ALD growth per cycle of HfO_2 and ZrO_2 was 0.109 and 0.097 nm, respectively, resulting in a slightly Hf-rich composition of $Hf_{0.58}Zr_{0.42}O_2$. Note that our prior work on a composition series across HfO_2 to ZrO_2 showed that a similar 1:1 Hf/Zr ALD cycle ratio process resulted in a 20 nm thick ferroelectric HZO film with high remanent polarization and low leakage current and motivates the usage of this composition in this study.[11] Following HZO deposition, a rapid thermal anneal was performed at 600 °C for 30 s in an N_2 environment. Films were heated at a rate of ∼20 °C/s. The sample was then diced and different electrodes were applied for the various experiments. By processing in this manner, the HZO composition and thermal history were held constant and differences could be attributed to the electrode/HZO electronic structure.

The deposition of the top electrode depended on the needs of the analytical technique. For IPE measurements, the photoresist was deposited and patterned, followed by either e-beam evaporation of approximately 10 nm of either Au, Al, Ta, Pt, or Pt/Ti (8.5 nm of Pt with 1.5 nm Ti as an adhesion layer) using a Temescal FC-2000 or sputter deposition of 10 nm TaN in a Denton Discovery 550 using a TaN target at room temperature in Ar. Finally, 75−200 μm diameter circular top electrodes of these metals were formed via a liftoff process. For XPS measurements, blanket films of TaN, Pt, Au, Ni, and Al were prepared with thicknesses described below. Metal layers for HAXPES measurements were deposited via radio frequency sputtering using a Lesker Lab 18 instrument through a shadow mask to define 10 nm thick, 2 mm square pads of Pt and Au.

Ferroelectricity was established in the devices prepared for IPE via polarization-field measurements made using a Radiant Technologies Precision LC II Ferroelectric Tester with a 1 ms measurement period. The resulting polarization hysteresis responses are shown in Figure 1. The magnitudes of the polarization are significantly lower than typically observed for this composition of HZO suggesting that the films are not predominately ferroelectric. This is attributed to the necessity of processing these films without a postmetallization anneal to maintain continuous, optically transparent electrodes for the IPE measurements. Regardless, each film showed a hysteretic response and clear polarization saturation was observed for most electrodes.

https://doi.org/10.1021/acsami.0c17729
ACS Appl. Mater. Interfaces 2021, 13, 14634−14643

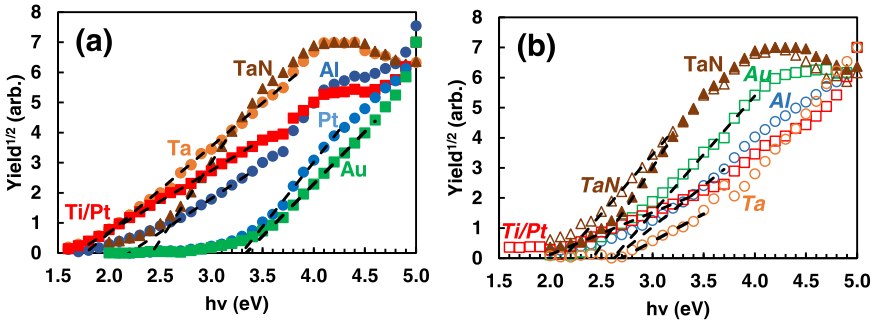

Figure 2. Representative $Y^{1/2}$ vs $h\upsilon$ plots for HZO MIM devices for emission from the (a) Au, Pt, Al, Ta, and Ti/Pt top electrodes as well as (b) the TaN bottom electrode (open symbols) for all devices, with the TaN top electrode (solid triangles) included for comparison. The dashed lines indicate the linear regressions that were used to determine the field-dependent φ_{thresh} value. Data were taken at approximately |0.75| MV/cm, except for Au (approximately 1.1 MV/cm).

IPE measurements of barrier heights were conducted using a homebuilt system. Light from a 150 W Xe arc lamp was passed through a monochromator to select a single wavelength to reach the MIM test device. Using a probe station, a voltage was applied to the bottom (TaN) electrode of the test device and the top electrode was grounded. Application of a positive (negative) voltage to the bottom electrode would result in net electron emission from the top (bottom) electrode to the conduction band of the HZO for transport to the opposite electrode. At each applied voltage, the monochromator swept the photon energy, $h\upsilon$, from 2 to 5 eV and the current, I, was measured. In some cases, photon energies as low as 1.5 eV and as high as 6.0 eV were used (indicated in the text). The current was normalized by subtracting the dark current for each applied bias and then converted to quantum yield, Y. Using an algorithm, the spectral threshold, φ_{thresh} (the photon energy at the onset of IPE), at each insulator electric field, E, was extrapolated from the most linear region of $Y^{1/2}$ vs $h\upsilon$ curves to the baseline x-intercept.[25] The square root of Y was used to account for the energy distribution of carriers in the metal electrode. E was corrected for the built-in field, E_{bi}, that arises due to the effective work function difference of the metal electrodes and was taken as the field at which electron emission switches from the top to the bottom electrode. Finally, to correct for any image force or field-induced barrier lowering that may be present, zero-field barrier heights, φ_{Bn}, were extrapolated from Schottky plots of the φ_{thresh} values vs $E^{1/2}$. IPE φ_{Bn} values have an estimated accuracy of ±0.1 eV.[14,20,25]

Lab-based XPS was conducted using a Kratos AXIS Supra instrument with a monochromatic Al Kα X-ray source and a hemispherical analyzer. The spot size was an elliptical 300 by 700 μm. Multiple locations on a given sample were analyzed to evaluate consistency across the surface. Core level peak positions varied by only 0.1 eV across any given surface. High-resolution spectra (pass energy 20 eV) were acquired with 20−50 meV step sizes. At this pass energy, the Kratos instrument has an energy resolution of 0.55 eV with Al Kα radiation. The valence band offsets (VBOs) between various metals and HZO were determined using the three-sample method as originally described by Kraut et al.[26−28] Samples were grounded to the sample holder using conductive silver paint. Blanket metal films of 0, 20, and 2 nm were used to measure the core level to the valence band of the HZO, top metal, and the difference between the core levels of the metal and HZO, respectively. For HZO, the Hf 4f and Zr 3d were measured as well as the valence band. For the metals, the following core peaks were used: Ta 4f, Al 2p, Pt 4f, or Au 4f.

HAXPES measurements were performed at the National Institute of Standards and Technology beamline 7-ID-2 at the National Synchrotron Light Source-II, Brookhaven National Laboratory. The beamline is equipped with a double crystal monochromator (DCM) for photon energy selection and a 200 mm radius concentric hemispherical electron analyzer (CHA) oriented with the center of the acceptance cone parallel to the photon polarization vector. Measurements were made at two photon energies to provide different probe depths: 2010 and 6007 eV. A small component of the third-order beam was present in the 2010 eV measurement, but peak shapes and positions were checked to verify that no third-order signal interfered with the primary photopeaks. Depth sensitivity is dependent on the photoelectron inelastic mean free path, which for Hf 4f electrons in Pt are 2.0 ± 0.3 nm at 2010 eV photon energy and 4.8 ± 0.7 nm at 6007 eV photon energy, as calculated by the TPP-2M formula.[29] For 2010 eV photon energy, Si(111) crystals were used in the DCM and the CHA pass energy was set to 50 eV; for 6007 eV photon energy, Si(220) crystals were used in the DCM and the CHA pass energy was set to 200 eV. Under these conditions, the experimental energy broadening is estimated to be 0.25 eV for 2010 eV photon energy and 0.58 eV for 6007 eV photon energy, as determined from the full width at half-maximum of a Gaussian function convolved with a step function fit to the Fermi edge of a gold film. The CHA was operated in an angular mode for all measurements to minimize the effect of beam alignment on the detector transmission function.[30] Further details of the beamline and endstation have been published previously.[31] HAXPES was performed on Pt/HZO and Au/HZO samples. For HAXPES barrier height calculation using the Kraut method, only two samples for each respective interface are necessary, since a relatively thick (10 nm) metal contact may be deposited on the HZO. The X-ray energy was tuned to obtain the XPS spectra from either (i) only the metal (using low energy 2010 eV X-rays) or (ii) both the metal and the underlying HZO (using higher energy 6007 eV X-rays). For the HZO reference sample, data was collected from a spot several mm away from the nearest electrode. HAXPES samples were mounted on a metal sample holder with conductive copper tape for electrical contact to the back side. To ensure the beam spot was centered on the electrode, the sample position was scanned across the 2 mm electrode to maximize the metal core line of interest while simultaneously minimizing the Hf 4f signal, which may arise from uncovered HZO. Samples were mounted at a 15° incident angle (75° takeoff angle).

RESULTS AND DISCUSSION

Shown in Figure 2 are representative plots of $Y^{1/2}$ vs $h\upsilon$ of HZO MIM devices taken at an applied field of |0.75 MV/cm| for Pt, Al, Ta, and Pt/Ti top electrodes and TaN bottom electrodes, and |1.1 MV/cm| for Au top electrodes. Several features merit comment. Tailing of the $Y^{1/2}$ vs $h\upsilon$ curve at low photon energies is typically seen for IPE of metal/insulator interfaces and may be due to either conduction band tailing in the HZO insulator, as was previously reported for HfO_2 and ZrO_2,[32] or the presence at the injecting interface of either an interfacial layer or laterally nonuniform trapped charge. The discontinuity seen at around 3.6 eV is a measurement artifact associated with the filter being changed at this photon energy.

The $Y^{1/2}$ vs $h\upsilon$ plots in Figure 2 appear to show an increase in slope at around 4.6−4.9 eV. To investigate, the photon

https://doi.org/10.1021/acsami.0c17729
ACS Appl. Mater. Interfaces 2021, 13, 14634−14643

energy for the Pt top electrode device was extended out to $h\nu$ = 6 eV in Figure 3. A large secondary increase in yield is

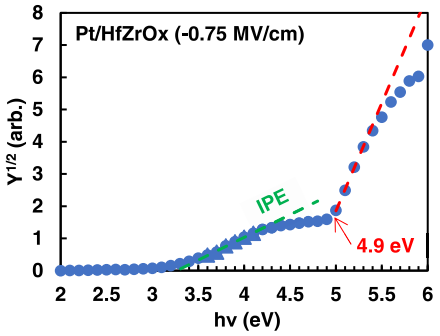

Figure 3. Representative $Y^{1/2}$ plot for emission from the Pt electrode with the $h\nu$ range extended to 6 eV. The dashed lines show the onset of IPE (green), and the potential onset of photoconduction (red).

apparent. From the intersection of a linear regression of this secondary slope to the baseline IPE slope, the onset is estimated to be about 4.9 eV.[14,33] (Note that although a single data point at 6 eV shows another uptick in yield, one cannot reliably interpret this data point as our IPE system is unable to extend the measurement beyond 6 eV.)

Possible origins of the increase in yield at around 4.9 eV in Figure 3 include the onset of direct photoconduction in the HZO, subthreshold photoconduction due to the presence of band tail states in the HZO, or photoconduction due to photoemission from defects such as oxygen vacancies[32,34−40] close to the VB edge. The strong increase in yield at 4.9 eV occurs at a much lower energy than previous calculations and measurements of the band gaps of HfO_2, ZrO_2, and c-HZO (5.6−6, 5.4−5.8, and 5.4 eV, respectively), suggesting that photoconduction across the band gap of HZO is not the origin.[6,13−15,34] Recent spectroscopic ellipsometry measurements of an identically processed c-HZO film with a TaN bottom electrode show optical absorption features at 4.3 and 4.9 eV in addition to an indirect band gap of 5.2 eV.[41] The 4.9 eV defect band energy detected by spectroscopic ellipsometry is consistent with the onset of photoconduction in this work and suggests that it is the origin of the observed feature. (Additional details supporting this discussion may be found in the Supporting Information.)

To extract the zero-field barrier heights, φ_{Bn}, and to correct for image force barrier lowering that may be present, Schottky plots are shown in Figure 4 of the IPE φ_{thresh} values vs the electric field in the insulator, $|E|^{1/2}$. φ_{Bn} values are summarized in Table 1 and range from 2 eV for the Ti/Pt top electrode to 3.4 eV for Pt and Au. For Au, Al, and TaN electrodes with HZO, we find electron energy barriers of 3.3, 2.6, and 2.7 eV, respectively, each approximately 0.2 eV lower than for the respective HfO_2 barriers measured by Jenkins et al.,[20,25] pointing toward a slightly lower band gap for HZO as compared to HfO_2. Considering the TaN electrodes for the nominally symmetric device, IPE measurements yield φ_{Bn} = 2.7 and 2.5 eV for the bottom and top electrodes, respectively. For bottom electrode TaN with opposing Ta and Ti/Pt electrodes, φ_{Bn} values of 2.7 and 3.0 eV, respectively, are obtained. These TaN values are within the wide range of IPE values reported for as-deposited and annealed TaN_x/HfO_2 (2.1−3.0 eV).[42,43] Whereas barrier heights at semiconductor/insulator interfaces have been reported to be relatively insensitive to the deposition method,[14] metal/insulator interfaces can be more sensitive to processing conditions such as deposition method, temperature, and precursor chemistry and it is likely that the differences in φ_{Bn} we observe for TaN are due to differences in the interfacial region resulting from differences in processing and chemical reactivity of the top electrode.[13,14] The differences in the slope of the Schottky plots between the various TaN bottom electrodes also suggest differences in the near interfacial regions of each bottom TaN interface. (Additional comparison to previous IPE results may be found in the Supporting Information.)

Figure 5 shows representative core peaks and valence band XPS spectra for the case of Al on HZO. For the thick Al metal

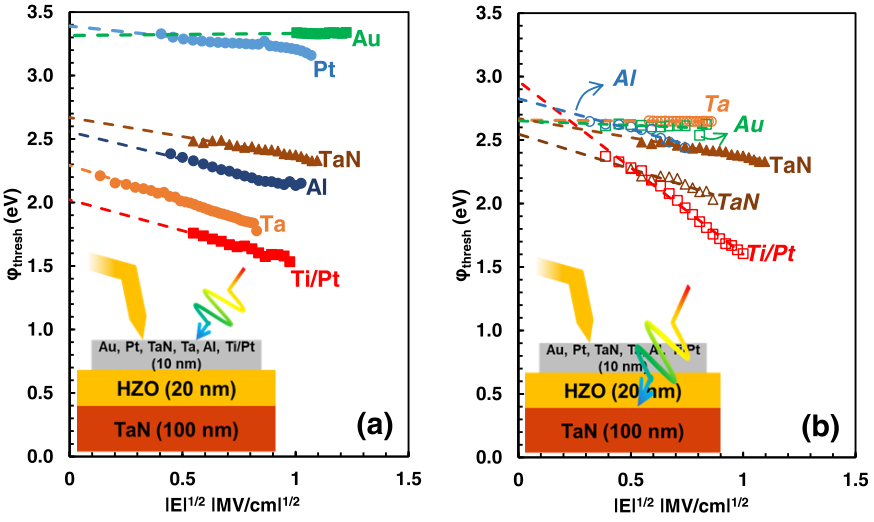

Figure 4. Schottky plots of φ_{thresh} vs $|E|^{1/2}$ for electrons emitted into the conduction band of the HZO from (a) all top electrodes and (b) all bottom TaN electrodes measured in this work. Linear regressions of the data are shown as dashed lines, with the y-intercepts giving the extracted φ_{Bn} for each metal. In (a), Au, Pt, Al, Ta, and Ti/Pt top electrodes are shown as closed symbols. In (b), TaN bottom electrodes are shown as open symbols with the shape matching that of the corresponding top electrode (italicized). For comparison, the top TaN electrode from (a) is copied in (b) using the same closed triangle.

https://doi.org/10.1021/acsami.0c17729
ACS Appl. Mater. Interfaces 2021, 13, 14634−14643

Table 1. Summary of Barriers Measured in This Work[a]

top electrode	Φ_M (eV)	IPE φ_{Bn} (eV)	XPS VBO (eV)	XPS φ_{Bn} (eV)	$\Delta\varphi_{Bn}$ IPE-XPS (eV)	HAXPES VBO (eV)	HAXPES φ_{Bn} (eV)	$\Delta\varphi_{Bn}$ IPE-HAXPES (eV)	$\Delta\varphi_{Bn}$ XPS-HAXPES (eV)	IPE $\varphi_{Bn,TaN}$ (eV)
Pt	5.65[b]	3.4	2.6	2.6	0.8	3.06	2.1	1.3	−0.5	2.7
Au	5.22[c]	3.3	3.44	1.8	1.54	3.08	2.1	1.2	0.4	2.7
Ti/Pt	4.33[b]	2								3.0
TaN	4.5[d]	2.7	3.5	1.7	1					2.5
Ta	4.25[b]	2.3	3.24	2.0	0.34					2.7
Al	4.28[b]	2.6	4.6	0.6	2					2.8
Ni	5.15[b]		3.31	1.9						

[a]Including metal work functions (Φ_M) from literature, IPE barrier heights, XPS valence band offsets, XPS determined barrier heights, the difference between IPE and XPS barrier heights, HAXPES VBOs, HAXPES φ_{Bn}, the difference between IPE and HAXPES barrier heights, the difference between XPS and HAXPES barrier heights, and the IPE barrier height of the opposing TaN bottom electrode. A HZO band gap of 5.2 eV was assumed. [b]Reference 47. [c]Reference 48. [d]Reference 49.

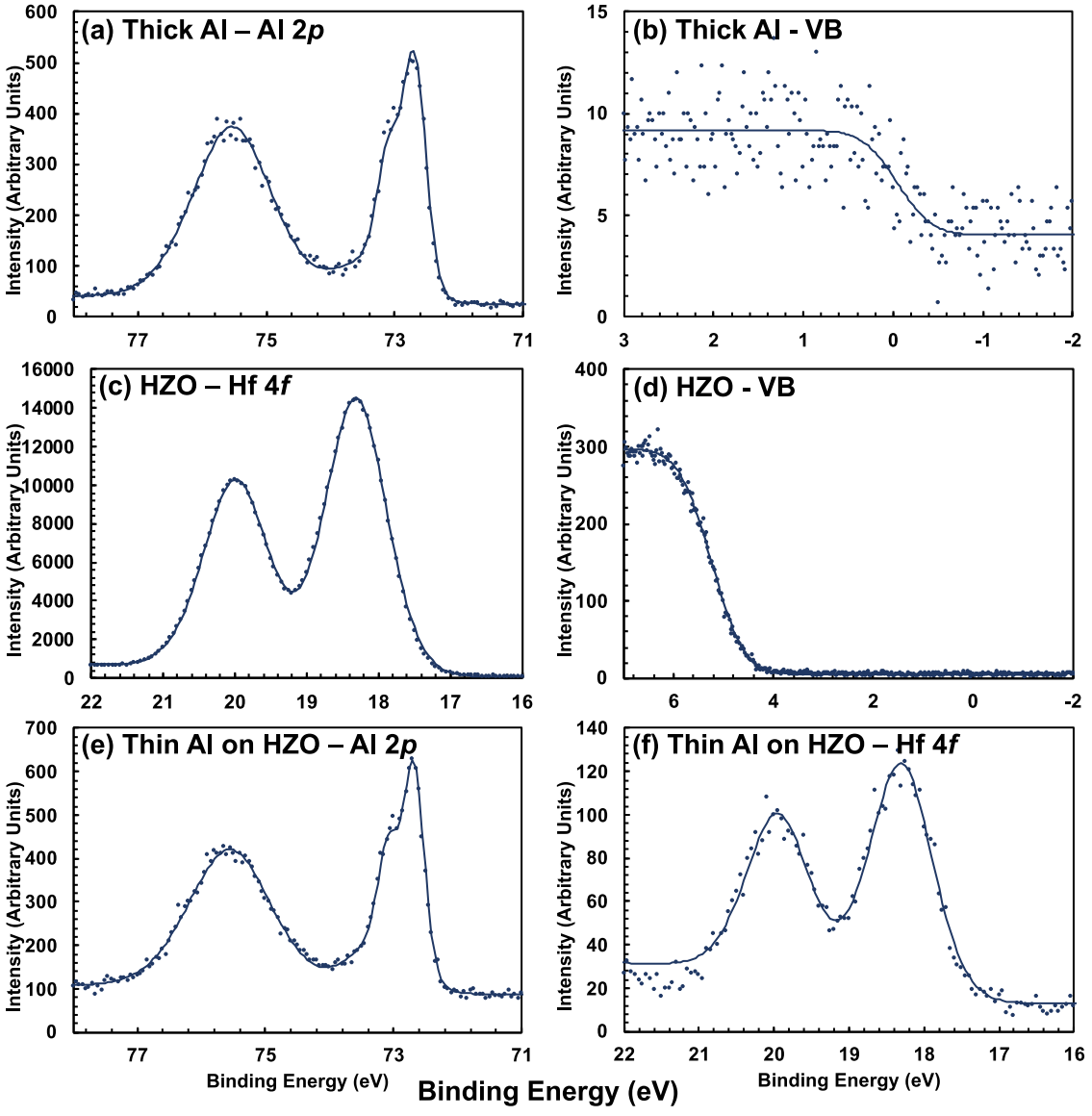

Figure 5. XPS spectra (*y*-axes in arbitrary units of intensity) showing (a) Al 2p and (b) Al VB for thick Al on HZO, (c) Hf 4f and (d) HZO VB for bare HZO, and (e) Al 2p and (f) Hf 4f for thin Al on HZO.

contact, the Al 2p core peak (Figure 5a) was measured along with the valence band (Figure 5b). The Al 2p peak in Figure 5a shows the typical doublet of the Al $2p_{3/2}$ and Al $2p_{1/2}$ for metallic Al, along with a large component at around 75.5 eV attributable to the native oxide at the Al surface. For TaN and Ta, the Ta 4f core peak was measured. For Au and Pt, the Au 4f and Pt 4f core peaks were measured, respectively. For Ni, the Ni 3s and Ni 3p peaks were both measured with no significant difference in the resulting calculated VBO. Peak positions were obtained by determining the peak maxima. The

https://doi.org/10.1021/acsami.0c17729
ACS Appl. Mater. Interfaces 2021, 13, 14634−14643

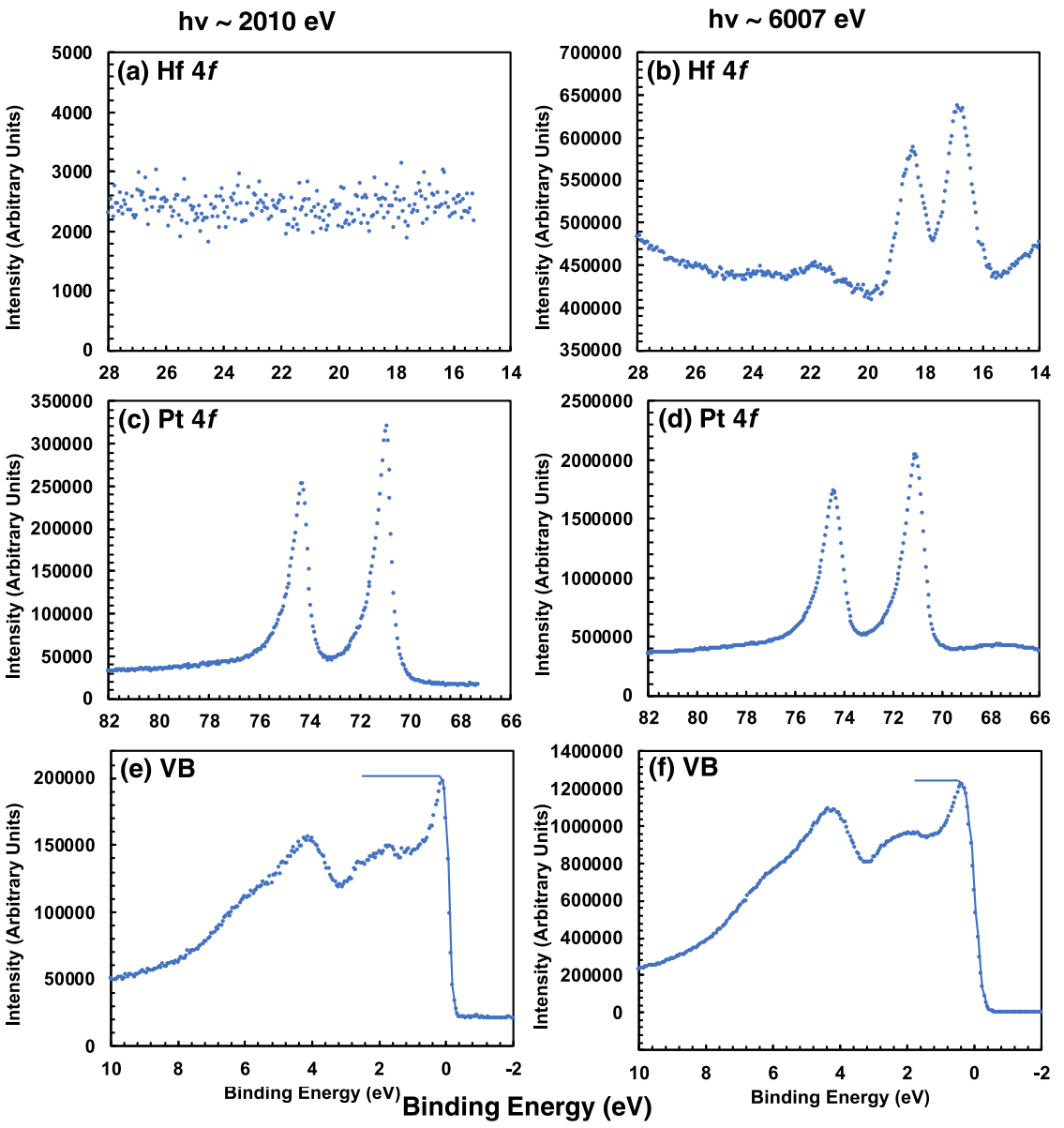

Figure 6. HAXPES photoemission spectra (*y*-axes in arbitrary units of intensity) for a sample with a 10 nm Pt film on HZO using low- and high-energy synchrotron X-rays. Shown are the Hf 4f signal for (a) 2010 and (b) 6007 eV; the Pt 4f signal for (c) 2010 and (d) 6007 eV; and the VB for (e) 2010 and (f) 6007 eV X-rays. The solid line in panels (e) and (f) show a Fermi step function fit to the data.

valence band edge for the thick metal contacts was a clear step function and the position of the edge was taken as the center of the step.[44] The edge shown in Figure 5b for Al has a poor signal to noise due to the native oxide which decreases counts at the valence band.

For the measurement of HZO as the substrate, either the Zr 3d or Hf 4f peaks (as shown in Figure 5c) could be used with no significant difference on the resulting calculated VBO. For example, for the HZO/Ta interface, the VBO was 3.24 ± 0.11 eV when using the Zr 3d, and 3.31 ± 0.10 eV when using the Hf 4f. In Figure 5d, the valence band of HZO was measured to determine the valence band maximum (VBM). The valence band was also fit with the Heaviside step function to determine the VBM which, for the case of nonmetals, is the energy at which photoemission ceases. The intersection point between the two linear regions defined by the steep valence band cutoff and a linear extrapolation of the baseline is estimated from the Heaviside fit. This method has generally been more repeatable for determining the position of the VBM as it accounts for a much greater number of data points than simple extrapolations of the two linear regions.[45] There are possibilities for error in the determination of peak positions and valence band edges; however, these errors are generally less than differences from sample-to-sample variability or heterogeneity across a given sample. The VBM of bare HZO was found to vary within 0.3 eV across samples from various depositions over several years. In this work, a self-consistent set of samples, including the bare HZO, was used for each VBO determination. Heterogeneity across a given sample could yield a deviation of ~0.1 eV in the VBO as determined from up to three points on each sample. The Hf 4f of HZO is shown in Figure 5c. In Figure 5e,5f, the Al 2p and Hf 4f peaks are for the thin Al sample.

Figure 6 shows the HAXPES photoemission spectra for the 10 nm Pt/HZO sample using both 2010 and 6007 eV X-rays. Shown in Figure 6a, the Hf 4f was not observed through the overlying 10 nm thick Pt using low energy 2010 eV X-rays

https://doi.org/10.1021/acsami.0c17729
ACS Appl. Mater. Interfaces 2021, 13, 14634−14643

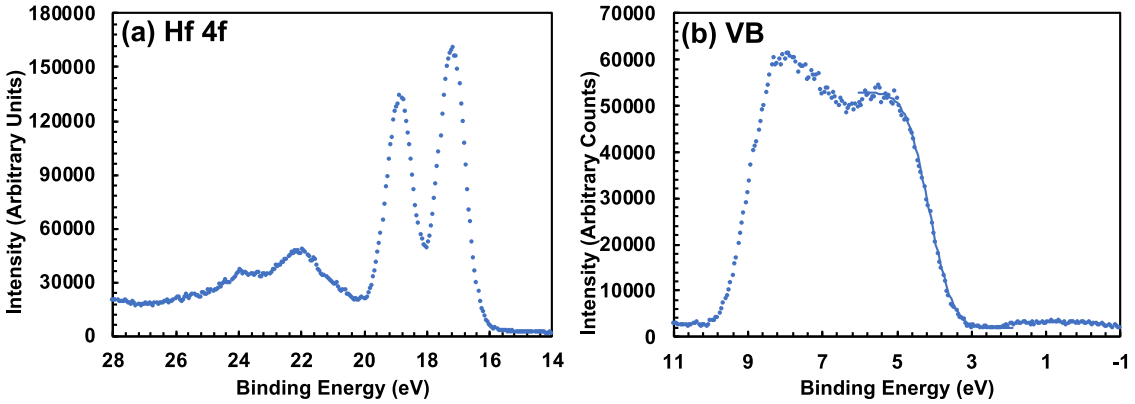

Figure 7. (a) Hf 4f peak and (b) VB of the bare HZO sample are shown from HAXPES at 6007 eV (*y*-axes in arbitrary units of intensity).

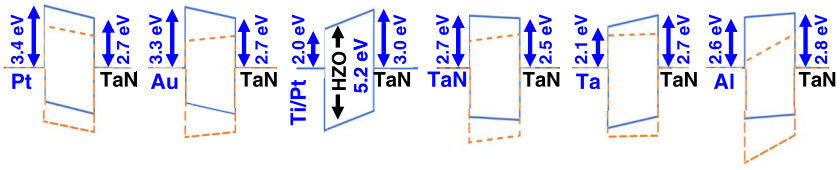

Figure 8. IPE (blue) and XPS (orange)-derived band diagrams. IPE φ_{Bn} values are shown. $E_{G,HZO}$ = 5.2 eV was assumed.

(since the information depth was less than 10 nm), whereas in Figure 6b, increasing the energy to 6007 eV reveals the presence of a Hf 4f signal, demonstrating that the buried HZO can be observed through the Pt overlayer. Thus, the Pt 4f (Figure 6c) and VB (Figure 6e) peaks of the Pt film measured using 2010 eV X-rays are representative of the "thick metal" sample required for the VBO determination, while the Hf 4f (Figure 6b) and Pt 4f (Figure 6d) measured using 6007 eV X-rays are representative of the "thin metal" sample. The VB is dominated by the overlying Pt contact for (e) 2010 and (f) 6007 eV X-rays. For the HZO reference, the Hf 4f signal was recorded at a spot several mm from the nearest metal electrode. Some small metal signal is present which may arise from either residual metal on the surface or the bottom TaN electrode, evident by the small signal at the Fermi level in Figure 7b; however, HZO valence band features dominate the spectrum and the VBM can be determined as above.

Summarized in Table 1 are barrier heights (φ_{Bn}) measured in this work by IPE, XPS, and HAXPES along with metal work functions (Φ_M) from literature. Band diagrams based on IPE and XPS results are shown in Figure 8, assuming a HZO band gap of 5.2 eV.[41] With the exception of the Ta interface, the estimated XPS barriers are significantly lower than the IPE barriers (0.8−2 eV) with an average offset of approximately 1.1 eV. The HAXPES ϕ_{bn} barrier values for Pt and Au are also much lower than the IPE values. The offset between the XPS and HAXPES vs IPE values is too large to be explained from any possible errors in the determination of energy positions for any of the techniques. The offset might be explained by the presence of a negative charge in the HZO. Possibilities include Ta ions in the HZO,[43] Hf^{3+} that forms to compensate for oxygen vacancies, remanent ferroelectric polarization charge at the surface, or process-induced damage. Neither lab-based XPS nor HAXPES revealed signatures for Hf^{3+}, though it could be present in a near interface region. The ferroelectric polarization is not likely to be the origin. The devices are nominally unpoled because they had not been subject to an electric field sufficiently greater than the coercive field. The lack of significant device-scale poling is supported by pyroelectric measurements on as-prepared TaN/HZO/TaN devices showing a response that is nearly an order of magnitude smaller than the poled value (4 $\mu C/m^2$ K as-prepared vs 27 $\mu C/m^2$ K after the measurement of a single hysteresis loop). During the IPE measurements of the barriers at the top electrode/HZO interface, the application of the electric field could align the ferroelectric polar vector toward the top electrode. This would result in a net positive charge in the dielectric at that interface that would act to lower the energy barrier. As a larger barrier is measured for the IPE measurements with respect to the XPS and HAXPES measurements, this cannot explain the difference. The presence of charge in the insulator can, however, lead to errors in estimating band alignment via XPS as the Kraut method for determining VBO with XPS assumes a constant energy for the vacuum level across the interface (HZO/metal). This charge is not a factor in the IPE method in which the externally applied bias allows a constant Fermi level across the interface.[14,46] Note that X-ray induced positive charging likely did not affect these results. Peak broadening, shifted spectra, or other distortions from charging were not observed. X-ray charging would result in larger rather than smaller barriers and thus cannot explain the systematic offset observed between XPS and IPE. X-ray charging also cannot explain the discrepancy in barrier heights between XPS and HAXPES as the change in VBO would be in the same direction (either larger or smaller) for both Au and Pt. As seen in Table 1, HAXPES measured a slightly higher VBO for Pt and a slightly lower VBO for Au. Note that a difference of +0.5 or −0.5 eV from photoemission is well within reason given the range of barrier heights plotted vs work function. It is more likely that the differences in VBO between HAXPES and XPS, which require two and three samples, respectively, are associated with differences in sample preparation and/or sample storage and handling. Besides X-rays, a likely source of oxide charging is during the sputtering or e-beam evaporation of the top electrodes. As is common in this field, no postmetallization anneal was performed to heal

https://doi.org/10.1021/acsami.0c17729
ACS Appl. Mater. Interfaces 2021, 13, 14634−14643

this damage and thus this is likely that process-induced charging is a source of the offset between IPE and XPS.

The IPE measured and lab-based XPS estimated HZO φ_{Bn} values are plotted in Figure 9 vs literature values of Φ_M for each electrode. It is seen that both XPS and IPE show essentially the same dependence of φ_{Bn} on Φ_M. In MIGS theory, intrinsic (induced) interface traps at the metal/insulator interface create an interfacial dipole that drives E_{FM} toward $E_{CNL,i}$ (the charge-neutral level of the insulator) so that the metal assumes an effective work function, $\Phi_{M,eff} = E_{CNL,i} + S(\Phi_{M,vac} - E_{CNL,i})$, where $\Phi_{M,vac}$ is the vacuum work function of the metal and the slope parameter, $S = d\varphi_{Bn}/d\Phi_{M,vac}$.[16,17] Ideal Schottky–Mott theory corresponds to $S = 1$ so that φ_{Bn} should be directly proportional to Φ_M, whereas when $S = 0$, E_{FM} is *pinned* at $E_{CNL,i}$. Empirically, it has been found that $S = 1/(1 + 0.1(\varepsilon_\infty - 1)^2)$ so that higher-κ dielectrics are expected to more effectively "pin" E_{FM} at $E_{CNL,i}$. For the HZO in this study, it is seen that the estimated S for the IPE data, based on the slope in Figure 9, is 0.84. For the XPS data, S is estimated to be 0.76. For both techniques, there is a larger degree of variation in the lower work function metals. Al is the biggest outlier for both techniques, perhaps due to interfacial layer formation and/or oxygen scavenging. Both the value of S and the significant scatter are consistent with previous reports of IPE barriers for HfO_2 and ZrO_2, which reported $S \approx 0.7$, and are an indication of nonidealities at the interfaces such as oxide charging, interfacial dipoles, and, especially for the reactive electrodes, interfacial layers.[14]

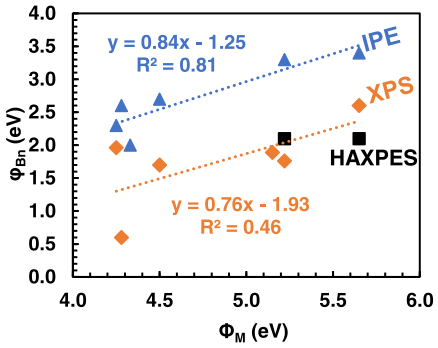

Figure 9. Plot of ϕ_{Bn} as determined via IPE (blue triangles), XPS (orange diamonds), and HAXPES (black squares) vs Φ_M. The dashed lines are linear least-squares fits used for determining the slope parameter, S.

Thus, despite the average 1.1 eV offset, ϕ_{bn} values derived using IPE and XPS show similar S values (0.84 vs 0.76), revealing the same qualitative trend of ϕ_{bn} on Φ_M. These results indicate that though HZO φ_{Bn} can be increased by increasing Φ_M, the change of φ_{Bn} is less than would be expected in the ideal Schottky–Mott model, suggesting that some Fermi level pinning (which reduces the impact of changes of work function) is present, as expected for a high-κ dielectric based on the MIGS theory.

SUMMARY AND CONCLUSIONS

Direct measurements of the energy barrier between various metal electrodes and the $Hf_{0.58}Zr_{0.42}O_2$ conduction band via IPE spectroscopy are reported for the first time. ALD HZO devices with TaN bottom electrodes and Al, Au, Ta, TaN, and Ti/Pt top electrodes all showed a clear hysteretic response, although polarization magnitudes were significantly smaller than typically reported due to a lack of a postmetallization anneal imposed by IPE sample requirements. For metals with which direct comparisons could be made, the barrier heights of HZO were consistently found to be 0.2 eV lower than for HfO_2. The onset of photoconduction was measured to be 4.9 eV, consistent with recent ellipsometric analysis, suggesting that this is a sub-band-gap defect band of this particular composition of crystalline HZO. Both IPE and XPS reveal the same qualitative dependence (S = 0.76–0.84) of the HZO energy barrier on metal work function, indicating that tuning through the choice of the metal electrode is possible. XPS and HAXPES-derived barriers, determined from band offsets measured using either the three-sample or two-sample method, respectively, were on average roughly 1.1 eV lower than IPE ϕ_{bn}, pointing to the presence of negative charge in the HZO film, potentially due to process damage incurred during top electrode deposition.

In summary, we find that HZO/electrode energy barriers can be tuned using metals with different vacuum work functions, but measured ϕ_{bn}'s are larger than predicted by the ideal theory (Φ_M–χ_i), indicating that metals behave as if they have a higher effective work function. Direct measurement of HZO-metal barriers using IPE is very useful for understanding device behavior and should help enable the integration of ferroelectric HfO_2-based devices into more complex devices and circuits.

ASSOCIATED CONTENT

Supporting Information

The Supporting Information is available free of charge at https://pubs.acs.org/doi/10.1021/acsami.0c17729.

Additional discussion including the origin of the 4.9 eV feature in Figure 3, a comparison of the measured HZO barrier heights with previous reports of HfO_2 barrier heights, and of image force barrier lowering and nonideal effects pertaining to the slopes of the Schottky plots in Figure 4 (PDF)

AUTHOR INFORMATION

Corresponding Author

John F. Conley, Jr. – *School of Electrical Engineering and Computer Science, Oregon State University, Corvallis, Oregon 97330, United States;* orcid.org/0000-0001-7407-9290; Email: jconley@eecs.oregonstate.edu

Authors

Melanie A. Jenkins – *School of Electrical Engineering and Computer Science, Oregon State University, Corvallis, Oregon 97330, United States;* orcid.org/0000-0002-9257-8250

Konner E. K. Holden – *School of Electrical Engineering and Computer Science, Oregon State University, Corvallis, Oregon 97330, United States;* orcid.org/0000-0002-9806-0014

Sean W. Smith – *Sandia National Laboratories, Albuquerque, New Mexico 87185, United States*

Michael T. Brumbach – *Sandia National Laboratories, Albuquerque, New Mexico 87185, United States*

M. David Henry – *Sandia National Laboratories, Albuquerque, New Mexico 87185, United States*

Conan Weiland – *Materials Measurement Science Division, Material Measurement Laboratory, National Institute of Standards and Technology, Gaithersburg, Maryland 20899, United States*

Joseph C. Woicik − *Materials Measurement Science Division, Material Measurement Laboratory, National Institute of Standards and Technology, Gaithersburg, Maryland 20899, United States*

Samantha T. Jaszewski − *Department of Materials Science and Engineering, University of Virginia, Charlottesville, Virginia 22904, United States;* orcid.org/0000-0002-4958-1219

Jon F. Ihlefeld − *Department of Materials Science and Engineering and Charles L. Brown Department of Electrical and Computer Engineering, University of Virginia, Charlottesville, Virginia 22904, United States;* orcid.org/0000-0003-0166-8136

Complete contact information is available at: https://pubs.acs.org/10.1021/acsami.0c17729

Author Contributions

The manuscript was written through the contributions of all authors. All authors have given approval to the final version of the manuscript.

Funding

J.F.C. Jr. and M.A.J. acknowledge the support of the NSF Center for Sustainable Materials Chemistry (Grant CHE-1606982). This work was conducted at the Materials Synthesis and Characterization (MaSC) Center, a National Nanotechnology Coordinated Infrastructure (NNCI) Northwest Nanotechnology Infrastructure (NNI) user facility at the Oregon State University which is supported in part by the National Science Foundation (Grant ECC-1542101) and Oregon State University. S.T.J. acknowledges support from the National Science Foundation's Graduate Research Fellowship Program (Grant DGE-1842490). This work was supported by the Laboratory Directed Research and Development Program at Sandia National Laboratories, a multimission laboratory managed and operated by National Technology & Engineering Solutions of Sandia, LLC, a wholly owned subsidiary of Honeywell International Inc., for the U.S. Department of Energy's National Nuclear Security Administration under Contract DE-NA0003525.

Notes

The authors declare no competing financial interest.

■ ACKNOWLEDGMENTS

The authors thank C. Tasker for equipment support and the Oregon Nanoscience and Microtechnologies Institute (ONAMI) for partial financial support. This paper describes objective technical results and analysis. Any subjective views or opinions that might be expressed in the paper do not necessarily represent the views of the U.S. Department of Energy or the United States Government. Commercial equipment, instruments, or materials are identified in this paper to specify the experimental procedure adequately. Such identification is not intended to imply recommendation or endorsement by the National Institute of Standards and Technology, nor is it intended to imply that the materials or equipment identified are necessarily the best available for the purpose. Official contribution is of the National Institute of Standards and Technology, not subject to copyright in the United States.

■ REFERENCES

(1) Salahuddin, S.; Datta, S. Use of Negative Capacitance to Provide Voltage Amplification for Low Power Nanoscale Devices. *Nano Lett.* **2008**, *8*, 405−410.

(2) Hoffmann, M.; Fengler, F. P. G.; Herzig, M.; Mittmann, T.; Max, B.; Schroeder, U.; Negrea, R.; Lucian, P.; Slesazeck, S.; Mikolajick, T. Unveiling the Double-Well Energy Landscape in a Ferroelectric Layer. *Nature* **2019**, *565*, 464−467.

(3) Hoffmann, M.; Pešić, M.; Chatterjee, K.; Khan, A. I.; Salahuddin, S.; Slesazeck, S.; Schroeder, U.; Mikolajick, T. Direct Observation of Negative Capacitance in Polycrystalline Ferroelectric HfO_2. *Adv. Funct. Mater.* **2016**, *26*, 8643−8649.

(4) Li, K.; Chen, P.; Lai, T.; Lin, C.; Cheng, C.; Chen, C.; Wei, Y.; Hou, Y.; Liao, M.; Lee, M.; Chen, M.; Sheih, J.; Yeh, W.; Yang, F.; Salahuddin, S.; Hu, C. In *Sub-60mV-Swing Negative-Capacitance FinFET without Hysteresis*, 2015 IEEE International Electron Devices Meeting (IEDM), 2015; pp 22.6.1−22.6.4.

(5) Mueller, S.; Summerfelt, S. R.; Muller, J.; Schroeder, U.; Mikolajick, T. Ten-Nanometer Ferroelectric Si:HfO_2 Films for Next-Generation FRAM Capacitors. *IEEE Electron Device Lett.* **2012**, *33*, 1300−1302.

(6) Ambriz-Vargas, F.; Kolhatkar, G.; Thomas, R.; Nouar, R.; Sarkissian, A.; Gomez-Yáñez, C.; Gauthier, M. A.; Ruediger, A. Tunneling Electroresistance Effect in a Pt/$Hf_{0.5}Zr_{0.5}O_2$/Pt Structure. *Appl. Phys. Lett.* **2017**, *110*, No. 093106.

(7) Böscke, T. S.; Müller, J.; Bräuhaus, D.; Schröder, U.; Böttger, U. Ferroelectricity in Hafnium Oxide Thin Films. *Appl. Phys. Lett.* **2011**, *99*, No. 102903.

(8) Starschich, S.; Schenk, T.; Schroeder, U.; Boettger, U. Ferroelectric and Piezoelectric Properties of $Hf_{1-x}Zr_xO_2$ and Pure ZrO_2 Films. *Appl. Phys. Lett.* **2017**, *110*, No. 182905.

(9) Müller, J.; Böscke, T. S.; Schröder, U.; Mueller, S.; Bräuhaus, D.; Böttger, U.; Frey, L.; Mikolajick, T. Ferroelectricity in Simple Binary ZrO_2 and HfO_2. *Nano Lett.* **2012**, *12*, 4318−4323.

(10) Riedel, S.; Polakowski, P.; Müller, J. A Thermally Robust and Thickness Independent Ferroelectric Phase in Laminated Hafnium Zirconium Oxide. *AIP Adv.* **2016**, *6*, No. 095123.

(11) Smith, S. W.; Kitahara, A. R.; Rodriguez, M. A.; Henry, M. D.; Brumbach, M. T.; Ihlefeld, J. F. Pyroelectric Response in Crystalline Hafnium Zirconium Oxide ($Hf_{1-x}Zr_xO_2$) Thin Films. *Appl. Phys. Lett.* **2017**, *110*, No. 072901.

(12) Park, M. H.; Lee, Y. H.; Mikolajick, T.; Schroeder, U.; Hwang, C. S. Review and Perspective on Ferroelectric HfO_2-Based Thin Films for Memory Applications. *MRS Commun.* **2018**, *8*, 795−808.

(13) Afanas'ev, V.; Kolomiiets, N.; Houssa, M.; Stesmans, A. Internal Photoemission Metrology of Inhomogeneous Interface Barriers. *Phys. Status Solidi A* **2017**, *215*, No. 1700865.

(14) Afanas'ev, V. V.; Stesmans, A. Internal Photoemission at Interfaces of High-κ Insulators with Semiconductors and Metals. *J. Appl. Phys.* **2007**, *102*, No. 081301.

(15) Robertson, J. Band Offsets of Wide-Band-Gap Oxides and Implications for Future Electronic Devices. *J. Vac. Sci. Technol., B* **2000**, *18*, 1785−1791.

(16) Tersoff, J. Schottky Barrier Heights and the Continuum of Gap States. *Phys. Rev. Lett.* **1984**, *52*, No. 465.

(17) Mönch, W. Role of Virtual Gap States and Defects in Metal-Semiconductor Contacts. *Phys. Rev. Lett.* **1987**, *58*, No. 1260.

(18) Lenahan, P. M.; Conley, J. F., Jr. What Can Electron Paramagnetic Resonance Tell Us about the Si/SiO_2 System? *J. Vac. Sci. Technol., B* **1998**, *16*, 2134−2153.

(19) Nguyen, N. V.; Kirillov, O. A.; Suehle, J. S. Band Alignment of Metal-Oxide-Semiconductor Structure by Internal Photoemission Spectroscopy and Spectroscopic Ellipsometry. *Thin Solid Films* **2011**, *519*, 2811−2816.

(20) Jenkins, M. A.; Klarr, T.; Austin, D. Z.; Li, W.; Nguyen, N. V.; Conley, J. F., Jr. Assessment of Energy Barriers Between ZrCuAlNi Amorphous Metal and Atomic Layer Deposition Insulators Using Internal Photoemission Spectroscopy. *Phys. Status Solidi RRL* **2018**, *12*, No. 1700437.

(21) Afanas'ev, V. V.; Stesmans, A.; Pantisano, L.; Cimino, S.; Adelmann, C.; Goux, L.; Chen, Y. Y.; Kittl, J. A.; Wouters, D.; Jurczak, M. TiNx/HfO_2 Interface Dipole Induced by Oxygen Scavenging. *Appl. Phys. Lett.* **2011**, *98*, No. 132901.
(22) Ludwig, W.; Kornefpel, B. Photoemission Studies on Thin Metal-Insulator-Metal Sandwiches. *Phys. Status Solidi B* **1967**, *24*, K137−K140.
(23) Gundlach, K. H.; Kadlec, J. Photoresponse of MIMIM Triodes. *Thin Solid Films* **1976**, *38*, 61−66.
(24) Kadlec, J.; Gundlach, K. H. Results and Problems of Internal Photoemission in Sandwich Structures. *Phys. Status Solidi A* **1976**, *37*, 11−28.
(25) Jenkins, M. A.; McGlone, J. M.; Wager, J. F.; Conley, J. F., Jr. Internal Photoemission Spectroscopy Determination of Barrier Heights between Ta-Based Amorphous Metals and Atomic Layer Deposited Insulators. *J. Appl. Phys.* **2019**, *125*, No. 055301.
(26) Kraut, E. A.; Grant, R. W.; Waldrop, J. R.; Kowalczyk, S. P. Precise Determination of the Valence-Band Edge in X-Ray Photoemission Spectra: Application to Measurement of Semiconductor Interface Potentials. *Phys. Rev. Lett.* **1980**, *44*, No. 1620.
(27) Waldrop, J. R.; Grant, R. W.; Kowalczyk, S. P.; Kraut, E. A. Measurement of Semiconductor Heterojunction Band Discontinuities by X-ray Photoemission Spectroscopy. *J. Vac. Sci. Technol., A* **1985**, *3*, 835−841.
(28) Waldrop, J. R.; Grant, R. W. Measurement of AlN/GaN (0001) Heterojunction Band Offsets by X-ray Photoemission Spectroscopy. *Appl. Phys. Lett.* **1996**, *68*, 2879−2881.
(29) Tanuma, S.; Powell, C. J.; Penn, D. R. Calculations of Electron Inelastic Mean Free Paths. V. Data for 14 Organic Compounds over the 50−2000 EV Range. *Surf. Interface Anal.* **1994**, *21*, 165−176.
(30) Weiland, C.; Browning, R.; Karlin, B. A.; Fischer, D. A.; Woicik, J. C. Note: Alignment/Focus Dependent Core-Line Sensitivity for Quantitative Chemical Analysis in Hard x-Ray Photoelectron Spectroscopy Using a Hemispherical Electron Analyzer. *Rev. Sci. Instrum.* **2013**, *84*, No. 036106.
(31) Weiland, C.; Jaye, C.; Quackenbush, N. F.; Gann, E.; Fu, Z.; Kirkland, J. P.; Karlin, B. A.; Ravel, B.; Woicik, J. C.; Fischer, D. A. NIST HAXPES at NSLS and NSLS-II. *Synchrotron Radiat. News* **2018**, *31*, 23−28.
(32) Lucovsky, G.; Seo, H.; Lee, S.; Fleming, L. B.; Ulrich, M. D.; Lüning, J.; Lysaght, P.; Bersuker, G. Intrinsic Electronically Active Defects in Transition Metal Elemental Oxides. *Jpn. J. Appl. Phys.* **2007**, *46*, No. 1899.
(33) Afanas'ev, V. V.; Stesmans, A.; Chen, F.; Shi, X.; Campbell, S. A. Internal Photoemission of Electrons and Holes from (100)Si into HfO_2. *Appl. Phys. Lett.* **2002**, *81*, 1053−1055.
(34) Alimardani, N.; King, S. W.; French, B. L.; Tan, C.; Lampert, B. P.; Conley, J. F., Jr. Investigation of the Impact of Insulator Material on the Performance of Dissimilar Electrode Metal-Insulator-Metal Diodes. *J. Appl. Phys.* **2014**, *116*, No. 024508.
(35) Grimley, E. D.; Schenk, T.; Sang, X.; Pešić, M.; Schroeder, U.; Mikolajick, T.; LeBeau, J. M. Structural Changes Underlying Field-Cycling Phenomena in Ferroelectric HfO_2 Thin Films. *Adv. Electron. Mater.* **2016**, *2*, No. 1600173.
(36) Starschich, S.; Menzel, S.; Böttger, U. Evidence for Oxygen Vacancies Movement during Wake-up in Ferroelectric Hafnium Oxide. *Appl. Phys. Lett.* **2016**, *108*, No. 032903.
(37) Lenahan, P. M.; Conley, J. F., Jr. Magnetic Resonance Studies of Trapping Centers in High-κ Dielectric Films on Silicon. *IEEE Trans. Device Mater. Reliab.* **2005**, *5*, 90−102.
(38) Campbell, J. P.; Lenahan, P. M.; Krishnan, A. T.; Krishnan, S. Identification of the Atomic-Scale Defects Involved in the Negative Bias Temperature Instability in Plasma-Nitrided p-Channel Metal-Oxide-Silicon Field-Effect Transistors. *J. Appl. Phys.* **2008**, *103*, No. 044505.
(39) Takeuchi, H.; Ha, D.; King, T.-J. Observation of Bulk HfO_2 Defects by Spectroscopic Ellipsometry. *J. Vac. Sci. Technol., A* **2004**, *22*, 1337−1341.
(40) Nguyen, N. V.; Davydov, A. V.; Chandler-Horowitz, D.; Frank, M. M. Sub-Bandgap Defect States in Polycrystalline Hafnium Oxide and Their Suppression by Admixture of Silicon. *Appl. Phys. Lett.* **2005**, *87*, No. 192903.
(41) Ihlefeld, J. F.; Luk, T. S.; Smith, S. W.; Fields, S. S.; Jaszewski, S. T.; Constantine, C.; Lu, P.; Henry, M. D.; Davids, P. S. Compositional Dependence of Linear and Non-Linear Optical Response in Crystalline Hafnium Zirconium Oxide Thin Films. *J. Appl. Phys.* **2020**, *128*, No. 034101.
(42) Afanas'ev, V. V.; Stesmans, A.; Pantisano, L.; Schram, T. Electron Photoemission from Conducting Nitrides (TiN_x,TaN_x) into SiO_2 and HfO_2. *Appl. Phys. Lett.* **2005**, *86*, No. 232902.
(43) Shamuilia, S.; Afanas'ev, V. V.; Stesmans, A.; Schram, T.; Pantisano, L. Internal Photoemission of Electrons from Ta-Based Conductors into SiO_2 and HfO_2 Insulators. *J. Appl. Phys.* **2008**, *104*, No. 073722.
(44) Fairley, N.; Carrick, A. *The Casa Cookbook*; Acolyte Science, 2005.
(45) Ihlefeld, J. F.; Brumbach, M.; Atcitty, S. Band Offsets of La_2O_3 on (0001) GaN Grown by Reactive Molecular-Beam Epitaxy. *Appl. Phys. Lett.* **2013**, *102*, No. 162903.
(46) Afanas'ev, V. V. Electron Band Alignment at Interfaces of Semiconductors with Insulating Oxides: An Internal Photoemission Study. *Adv. Condens. Matter Phys.* **2014**, *2014*, No. 301302.
(47) Michaelson, H. B. The Work Function of the Elements and Its Periodicity. *J. Appl. Phys.* **1977**, *48*, 4729−4733.
(48) Derry, G. N.; Kern, M. E.; Worth, E. H. Recommended Values of Clean Metal Surface Work Functions. *J. Vac. Sci. Technol., A* **2015**, *33*, No. 060801.
(49) Kang, C. S.; Cho, H.-J.; Kim, Y. H.; Choi, R.; Onishi, K.; Shahriar, A.; Lee, J. C. Characterization of Resistivity and Work Function of Sputtered-TaN Film for Gate Electrode Applications. *J. Vac. Sci. Technol., B* **2003**, *21*, 2026.

https://doi.org/10.1021/acsami.0c17729
ACS Appl. Mater. Interfaces 2021, 13, 14634−14643